7-1980

Half-Space Radiation by EMAT's

William J. Pardee
Rockwell International

R. B. Thompson
Rockwell International

Half-Space Radiation by EMAT's

Abstract
A Green's function calculation of the far field radiation patterns of EMAT's is presented. The approach is based upon (a) closed form expressions for the eddy current and static magnetic field distributions, established by the EMAT, which react to produce the driving Lorentz forces and (b) a Green's function derived from the steepest descent approximation to the far field response of an arbitary surface point force on a half space. Numerical results are presented, illustrating the radiation patterns of the three common EMAT designs. Included are vertically polarized shear waves as radiated by both meander coil and periodic magnet EMAT's and horizontally polarized shear waves as radiated by the latter.

Keywords
Nondestructive Evaluation

Disciplines
Materials Science and Engineering

HALF-SPACE RADIATION BY EMAT's

William J. Pardee and R.B. Thompson
Rockwell International Science Center
1049 Camino Dos Rios
Thousand Oaks, CA 91360

ABSTRACT

A Green's function calculation of the far field radiation patterns of EMAT's is presented. The approach is based upon (a) closed form expressions for the eddy current and static magnetic field distributions, established by the EMAT, which react to produce the driving Lorentz forces and (b) a Green's function derived from the steepest descent approximation to the far field response of an arbitary surface point force on a half space. Numerical results are presented, illustrating the radiation patterns of the three common EMAT designs. Included are vertically polarized shear waves as radiated by both meander coil and periodic magnet EMAT's and horizontally polarized shear waves as radiated by the latter.

INTRODUCTION

Electromagnetic acoustic transducers (EMAT's) have several features which are very useful in ultrasonic NDE. These features include non-contact operation, which permits high speed inspection and inspection of hot parts such as welded plates, the ability to produce beams of easily controlled polarization (including especially horizontally polarized shear waves), and the production of a beam which can be electronically scanned in angle. The increasing importance of these properties for both materials science studies (e.g., residual stress, microstructure) and ultrasonic scattering NDE has made quantitative knowledge of their radiation patterns desirable.

Three dimensional calculations of these radiation patterns in the far field are presented on this paper for three types of EMAT's radiating into a half-space. Two of the EMAT's consist of periodically polarized magnets surrounded by solenoidal coils to produce, respectively, shear-horizontal (SH) and shear vertical (SV) bulk waves. The third consists of a uniformly polarized magnet and periodic meander coil which produces SV bulk waves. The computations differ from earlier treatments (1,2) of EMAT radiation patterns in several respects. All three components of the surface tractions are calculated directly from Maxwell's equations, based on the assumption that the transducer currents and magnetization are uniform. The very important effects of non-uniformity in the fields and eddy currents are thereby explicitly included, making it possible later to obtain a quantitative measure of the modal purity of the generated wave. Second, these calculations are done for rectangular (rather than cylindrical(2) EMAT's. Third, the lateral (three dimensional) variation of the EMAT beam is obtained.

The paper is divided into three major parts; the solution of Maxwell's equations to obtain the eddy current and static fields for the three types of EMAT, the calculation of the far field response to an arbitrary (three-dimensional) point force on the surface of a half-space, and the combination of these results to obtain the (non-point force) elastic wave radiation from the three types of EMAT. The point force response (Green's function) of the half-space is obtained analytically, as are the surface tractions, while the combination is evaluated numerically.

THE EMAT SURFACE TRACTIONS

The three types of EMAT considered here are illustrated in Fig. 1. In a convenient, although somewhat non-uniform terminology, the periodic magnet, longitudinal coil EMAT (upper left) will be referred to as SH (because it generates SH waves), the periodic magnet, transverse coil (upper right) as SV, and the single magnet, meander coil (which also generates SV waves) will be referred to as the MC EMAT. The current loops for the periodic permanent magnet EMAT's are schematically illustrated loosely wound, but are assumed to be a tightly wrapped (uniform sheet) coil in the calculations below. The coordinate system used throughout this paper will be right-handed, with the EMAT centered under the origin (the elastic waves are generated in a metal occupying the half-space $z > 0$), with the periodic variation (magnet or meander coil) along the x axis.

Calculation of Static Field

Consider first a single uniformly magnetized permanent magnet located at $-L/2 < x < L/2$, $-w/2 < y < w/2$, and $-(s+h) < z < -s$, as shown in Fig. 2. The magnetic field is readily obtained from classical magnetostatics. With uniform magnetization $\underset{\sim}{M} = M_0 \underset{\sim}{z}$, we have

$$\nabla \cdot H = -\mu_0^{-1} \nabla \cdot M = (M_0/\mu_0)[\delta(z+s) - \delta(z + s + h)] \qquad (1)$$

Since the field is static, $\nabla \times \underset{\sim}{H} = 0$, and we can find $\underset{\sim}{H}$ from a potential Φ_M.

$$\underset{\sim}{H} = -\nabla\Phi_M \quad , \tag{2}$$

which satisfies Poisson's equation,

$$\nabla^2\Phi_M = \rho_M = \nabla\cdot\underset{\sim}{M}/\mu_o \quad . \tag{3}$$

The result is

$$\Phi_M(\underset{\sim}{r}) = -\int d^3r'\rho_M(\underset{\sim}{r}')/(4\pi R) \tag{4}$$

$$\text{or} \quad \underset{\sim}{H}(\underset{\sim}{r}) = -\int d^3r' R\, \rho_M(\underset{\sim}{r}')/(4\pi R^3) \tag{5}$$

$$\text{where} \quad \underset{\sim}{R} = \underset{\sim}{r} - \underset{\sim}{r}' \tag{6}$$

and $R = (\underset{\sim}{R}\cdot\underset{\sim}{R})^{1/2}$. The integrals are two dimensional over the top and bottom surfaces of the magnet. The results for the top surface are conveniently written as double sums of two terms each, and with $\underset{\sim}{B} = \mu_o\underset{\sim}{H}$.

$$B_x = M_o/(4\pi) \sum_{m,n=1}^{2} (-1)^{m+n} \log (y_n + R_{mn}) \quad , \tag{7}$$

$$B_y = M_o/(4\pi) \sum_{m,n=1}^{2} (-1)^{m+n} \log (x_m + R_{mn}) \quad , \tag{8}$$

and

$$B_z = M_o/(4\pi) \sum_{m,n=1}^{2} (-1)^{n} \tan^{-1}(x_m y_n/[sR_{mn}]) \quad . \tag{9}$$

with

$$x_m = -[x + (-1)^m L/2] \quad , \tag{10}$$

$$y_n = -[y + (-1)^n w/2] \quad , \tag{11}$$

and

$$R_{mn} = (x_m^2 + y_n^2 + s^2)^{1/2} \quad . \tag{12}$$

The contribution from the bottom surface is obtained from Eq. (7-9) by the substitutions $M_o \to -M_o$, $s \to s + h$. These expressions will be used in predicting the performance of the MC EMAT.

For the SH and SV EMAT's the periodic magnet field can be obtained by summing contributions like those above with alternating sign, but it is preferable to take the magnet pair (Fig. 3) as the fundamental unit. The procedure is identical, though the integrals are somewhat longer. The results are, for the near surface,

$$B_x = M_o/(4\pi) \sum_{m,n=1}^{2} \text{sgn}(y_n)\log\left\{(Y_n - R_{2m-1,n})\right.$$

$$\left.(Y_n + R_{2,n})/\,[(Y_n + R_{2m-1,n})(Y_n - R_{2,n})]\right\} \tag{13}$$

$$B_y = M_o/(4\pi) \sum_{m=1}^{3} (3 \bmod(m,2)-2)\log\,[(x_m + R_{m,1})/$$

$$(x_m + R_{m,2})] \tag{14}$$

and

$$B_z = M_o/(8\pi) \sum_{n=1}^{2} \sum_{m=1}^{3} (2-3 \bmod(m,2)) \tan^{-1}$$

$$(Y_n\, x_m/(sR_{mn})) \quad . \tag{15}$$

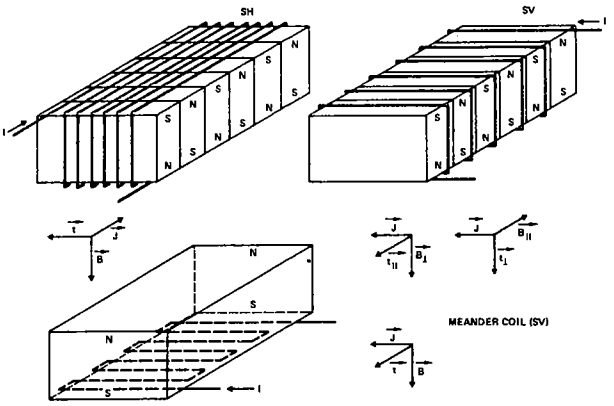

Fig. 1 The three EMAT configurations with the eddy currents, magnetic fields, and resulting forces schematically illustrated.

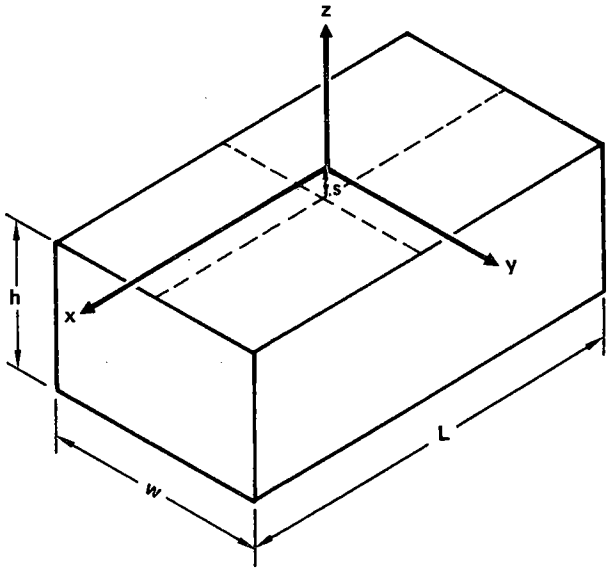

Fig. 2 Geometry for calculating the static field of a single permanent magnet such as used in the meander coil EMAT.

In the foregoing (Eq. 13-15) the expressions for y_n are given by Eq. (11) and

$$Y_n = |y_n|, \tag{15a}$$

but there are now three x values,

$$x_m = (m-1)D/2 - x \quad , \; m = 1, 2, 3 \quad , \tag{16}$$

and the factor 3 mod(m,2)-2 is just the set of weights 1, -2, 1. With this convention, R_{mn} is still given by Eq. (12). The contribution from the lower (distant) surface can be obtained as before, but this is small, and is commonly made to vanish, in practice, by connecting the magnets with a soft iron shunt. One qualitative feature to be noted is the presence in the components of the static field parallel to the surface (B_x and B_y) of logarithmic singularities at each magnet boundary (Eqs. (13) and (14) evaluated for s = 0).

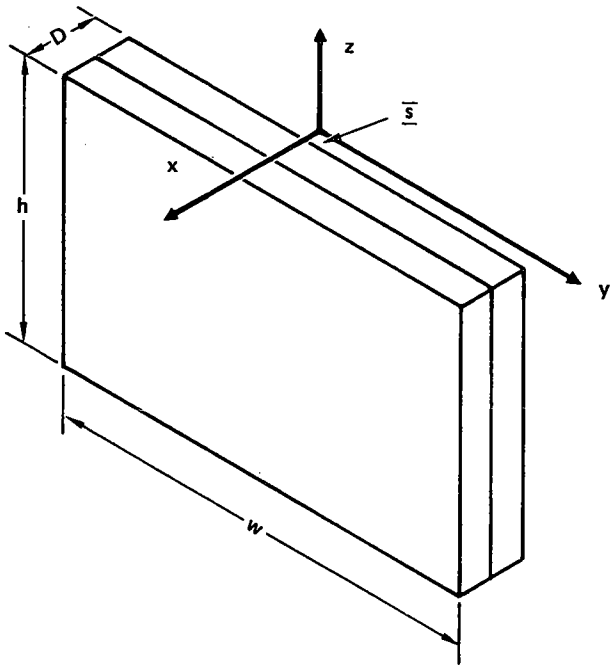

Fig. 3 Geometry for calculation of the static field of a single permanent magnet pair (quadrupole) which will be repeated perodically to form the SM and SV EMAT's.

Eddy Currents Induced by a Rectangular Current Loop

For the frequencies of interest (~1 MHz) and in highly conducting metals such as aluminum, the wavelength of the elastic waves is much greater than the skin depth, so the eddy currents can be treated as a surface current distribution (amps/meter),

$$\underset{\sim}{K}(x,y) = \int_0^\infty dz\, \underset{\sim}{J}(x,y,z) \qquad (17)$$

By applying the Maxwell equations for $\nabla \times \underset{\sim}{H}$ to a small planar closed path along a vector $\underset{\sim}{u}$ parallel to the metal surface, one obtains

$$\int \underset{\sim}{H}\cdot d\underset{\sim}{l} = \underset{\sim}{H}\cdot\underset{\sim}{u} = \underset{\sim}{K}\cdot\hat{\underset{\sim}{n}} \times \underset{\sim}{u} \ , \qquad (18)$$

where $\hat{\underset{\sim}{n}}$ is normal to the surface. The most general vector $\underset{\sim}{u}$ parallel to the surface can be written in the form $\underset{\sim}{u} = \underset{\sim}{a} \times \hat{\underset{\sim}{n}}$ where $\underset{\sim}{a}$ is arbitrary. Inserting this in Eq. (18) yields the condition,

$$\underset{\sim}{H}\cdot\underset{\sim}{a} \times \hat{\underset{\sim}{n}} = \underset{\sim}{K}\cdot\underset{\sim}{a} \ , \qquad (19)$$

$$\text{or} \quad \underset{\sim}{K} = \underset{\sim}{H} \times \hat{\underset{\sim}{n}} \ , \qquad (20)$$

and this enables one to obtain the surface current $\underset{\sim}{K}$ from the field $\underset{\sim}{H}$. The field $\underset{\sim}{H}$ for the rectangle loop of the SH EMAT, shown in Fig. 4 is obtained from the Biot-Savart law,

$$d\underset{\sim}{B} = \mu_0 dI\, d\underset{\sim}{l} \times \underset{\sim}{R}/(4\pi R^3) \qquad (21)$$

where R is as in Eq. (6), dI = I dy/b, and $d\underset{\sim}{l}$ is either $\hat{\underset{\sim}{e}}_1 dx$ or $\hat{\underset{\sim}{e}}_3 dz$. To satisfy the condition that the normal component of $\underset{\sim}{B}$ vanishes at the conductor surface, an image contribution must be included. The effect of the image is to double the parallel components. The results are

$$K_x = -K_o \sum_{i,j,k=1}^{2} (-1)^{i+j+k} \left\{ \tan^{-1}\left[x_i y_j/(z_k R_{ijk})\right] + \tan^{-1}\left[y_j z_k/(x_i R_{ijk})\right] \right\} \ , \qquad (22)$$

$$K_y = K_o \sum_{i,j,k=1}^{2} (-1)^{i+j+k} \log(z_k + R_{ijk}) \ , \qquad (23)$$

where

$$K_o = NI/(2\pi b) \ , \qquad (24)$$

$$x_i = x + (-1)^{i+1}\, a/2 \ , \qquad (25)$$

$$y_i = y + (-1)^{j+1}\, b/2 \ , \qquad (26)$$

$$z_k = z + (2 - k)c \ , \qquad (27)$$

and

$$R_{ijk} = (x_i^2 + y_j^2 + z_k^2)^{1/2} \ . \qquad (28)$$

For the SV EMAT, the coil is rotated 90° about the z-axis and the same results hold after the appropriate rotation.

Eddy Currents Induced by a Meander Coil Segment

The meander coil primitive segment is shown in Fig. 5. The induced surface currents are calculated as for the rectangular loop of §2.2, but now require only one-dimensional integrals. The results are

$$K_x/K_o = \left(\frac{x_2}{R_{22}} - \frac{x_1}{R_{12}}\right)\frac{1}{y_2^2+h^2} + \left[\left(\frac{x_3}{R_{31}} - \frac{x_2}{R_{21}}\right)\frac{1}{y_1^2+h^2}\right], \qquad (29)$$

$$K_y/K_o = \left(\frac{y_2}{R_{12}} - \frac{y_1}{R_{11}}\right)\frac{1}{x_1^2+h^2} + \left(\frac{y_1}{R_{21}} - \frac{y_2}{R_{22}}\right)\frac{1}{x_2^2+h^2} \ , \qquad (30)$$

where

$$K_o = \mu_o Ih/(2\pi) \quad , \tag{31}$$

$$x_n = x + (3 - 2n)\alpha/2 \quad , \tag{32}$$

$$y_m = y - (-1)^m \beta/2 \quad , \tag{33}$$

and

$$R_{nm} = (x_n^2 + y_m^2 + h^2)^{1/2} \quad . \tag{34}$$

α and β define the coordinates of the coil as described in the caption to Fig. 5. The term in square brackets in Eq. (29) is the only contribution from the conductor at $\alpha/2 < x < 3\alpha/2$, $y = -\beta/2$, and this is to be omitted from the rightmost periodic repetition of the primitive meander coil segment.

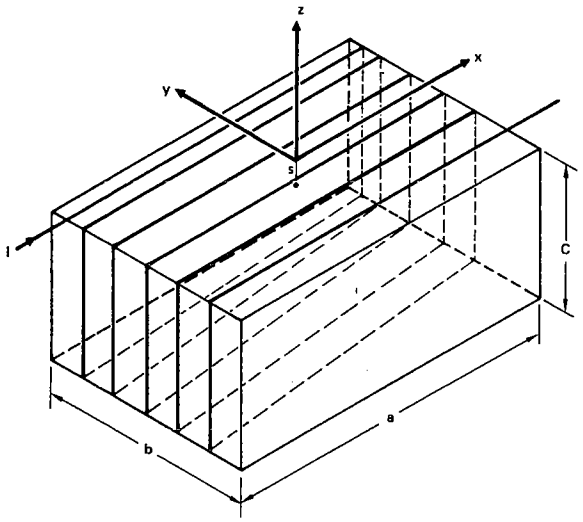

Fig. 4 Rectangular current loop of length a, width b, height c, located a distance s below the xy plane.

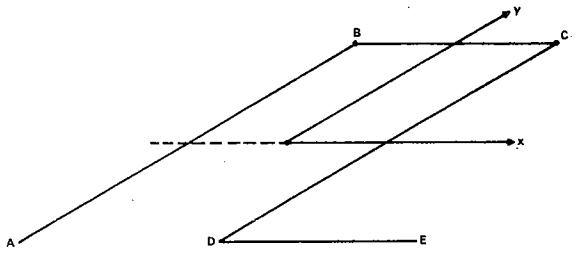

Fig. 5 One segment of a meander coil. Entire coil is built up by periodic repetition, with the last leg omitted from the last segment. The coordinates are A = 1/2 $(-\alpha, -\beta)$, B = 1/2 $(-\alpha, \beta)$, C = 1/2 (α, β), D = 1/2 $(\alpha, -\beta)$ and E = 1/2 $(3\alpha, -\beta)$.

The Surface Tractions

The Lorentz force per unit volume on the electrons, $\underset{\sim}{f} = \underset{\sim}{J} \times \underset{\sim}{B}$, has been shown[3-11] to be transferred to the lattice. By integrating over z the surface traction (force per unit area) is obtained,

$$\underset{\sim}{T} = \underset{\sim}{K} \times \underset{\sim}{B} \quad , \tag{35}$$

where it has been noted that the skin depth is small compared to both the variation in the static field, B, and the wavelength of the elastic waves. The symmetries of the currents, fields, and tractions are tabulated in Table 1. Note that the meander coil eddy currents have no symmetry in y. Three dimensional plots of the three components of surface traction for each of the three transducer types are shown in Figs. 6-14. The transducer parameters are given in Table 2. In interpreting the results, it is important to recall that the in-plane magnetic component perpendicular to a magnet boundary has a weak (logarithmic) singularity (~log s) at that boundary, as can be seen from, e.g., Eq. (8) for B_y at $y = w/2$. The expression is singular for $-D/2 < x < D/2$. i.e., along the magnet boundary. Moreover, the derivative with respect to y, $\partial B_y/\partial y$, changes rapidly in magnitude and reverses sign at the boundary. This is evident, for example, in $t_3 = K_x B_y - K_y B_x$ for the SV EMAT, Fig. 11.

Table 1

	SH		SV		MC	
	x	y	x	y	x	y
K_x	+	+	-	-	+	
K_y	-	-	+	+	-	+
H_x	+	+	+	+	+	-
H_y	-	-	-	-	+	-
H_z	-	+	-	+	+	+
t_x	+	-	-	+	-	+
t_y	-	+	+	-	+	
t_x	-	-	+	+	+	

Symmetries in x and y of the surface currents, static field and surface traction for the three varieties of EMAT shown in Fig. 1. K_x for the meander coil EMAT is neither symmetric or antisymmetric.

Table 2

SH and SV	
Length, mm	38.1
Width, mm	7.87
Height, mm	4.0
Liftoff, mm	0.254
Magnet period, mm	6.35
# Magnet pairs	6
MC	
Length, mm	31.75
Width, mm	7.87
Liftoff, mm	0.254
Coil period, mm	6.35
Magnet height, mm	4.0
# m.c. loops	6

The SH EMAT tractions (Figs. 5-7) exhibit two desirable properties: the desired component (t_y, Fig. 6) is very smooth and periodic, and the undesired components (t_x,t_z, Figs. 5, 7) are much smaller. These undesired stress components are a result of fringing fields at the edges of the magnet and coil structure. The dominant currents and fields are K_y and B_z which combine to produce the t_y illustrated in Fig. 7. The major contributions to undesired components arise from terms in the cross product of Eq. (35) which contain one fringing field and one of the dominant fields. Thus the t_x distribution arises from the term $K_y B_x$ which, as shown in Fig. 6, is largest at the end of the magnet array where the current K_y is fringing as part of the closed paths in which it must flow. The undesired t_z distribution shown in Fig. 8 arises from two terms. $K_y B_z$ is again largest at the magnet array ends due to the same fringing of K_y, while $K_x B_y$ is largest at the edges. The latter has a sign change due to the change in sign of K_x, occurring because the direction of the fringing eddy currents is opposite to those under the coil. The t_x and t_z components are reduced by 13 dB below the t_y component for this transducer.

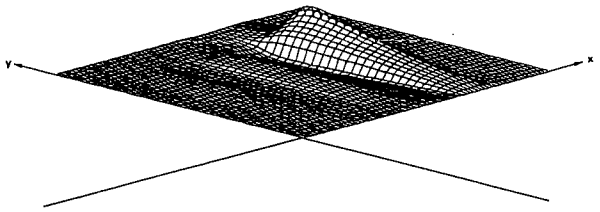

Fig. 6 Surface traction t_x (x,y) in first quadrant (x,y > 0) for SH EMAT. Scale in y direction expanded by factor of 5.

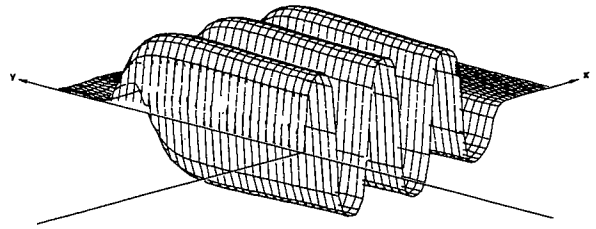

Fig. 7 Surface traction t_y (x,y) in first quadrant (x,y > 0) for SH EMAT. All scales identical to those of Fig. 6.

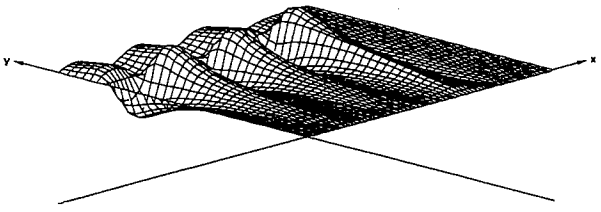

Fig. 8 Surface traction t_z (x,y) in first quadrant, (x,y>0) for SH EMAT. All scales identical to those of Fig. 6.

The SV EMAT generates elastic waves by a combination of t_x (Fig. 9) and t_z (Fig. 11) tractions; the undesired t_y (Fig. 10) component is much smaller. In this case, the periodic x and z components are strongly modulated. This is a consequence of the solenoid-like coil which induces very large eddy currents near its ends but only weak currents near its center because the magnetic fields are nearly entirely contained by the coil. In this case, the K_y, B_x, and B_z fields are dominant. The undesired t_y stress component shown in Fig. 10 is produced by the term $K_z B_x$. For this coil geometry, the fringing current K_x is greatest at the magnet array ends (coil edge), and produces the indicated stress, which is about 10 dB from the desired components. The strong modulation in the desired stress components for the SV case, in contrast to the highly periodic behavior for the SH case, arises because of the different aspect ratios of the solenoidal coils when wound transversely or longitudinally around the magnet array.

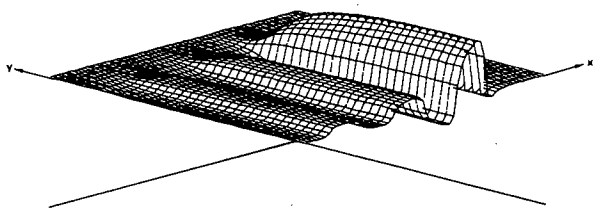

Fig. 9 t_x in first quandrant for SV EMAT. Transverse (y) scale expanded by a factor of 5.

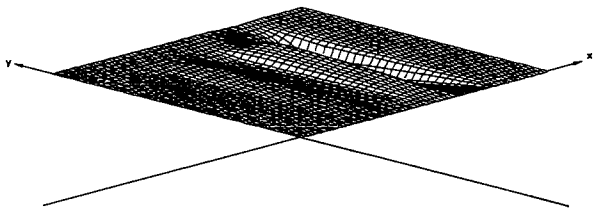

Fig. 10 t_y in first quandrant for SV EMAT. All scales as in Fig. 9.

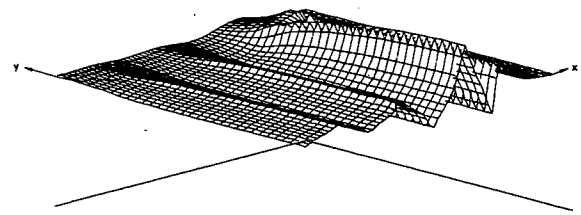

Fig. 11 t_z in first quandrant for SV EMAT. All scales as in Fig. 9.

The MC EMAT has singular behavior at both the wires and the magnet edges, as well as a lower amplitude traction (for given current and field) then the SV or SH magnets. It also lacks the symmetry (Table 1) of the other two EMAT types.

THE FAR-FIELD HALF-SPACE GREEN'S FUNCTION FOR A SURFACE SOURCE

The displacement field $u_m(t,\underline{r})$ satisfies

$$\rho \frac{\partial^2 u}{\partial t^2} m = \frac{\partial \sigma_{mn}}{\partial r_n} \qquad (36)$$

where

$$\sigma_{mn} = \lambda \frac{\partial u_j}{\partial r_j} \delta_{mn} + \mu \left(\frac{\partial u_m}{\partial r_n} + \frac{\partial u_n}{\partial r_m} \right) \qquad (37)$$

with λ and μ the Lamé constants and summation over $j = 1, 2, 3$ implied. At the surface ($z = 0$), the stresses satisfy

$$\sigma_{m3}(t,x,y,o) = T_m(t,x,y) \quad , \qquad (38)$$

with $\underline{I}$ given by Eq. (35). This general solution is most conveniently obtained by superposition of solutions $G_{mn}(\omega,\underline{r})$ for the special case in which

$$T_n(t,x,y) = t_n \exp(j\omega t)\delta(x)\delta(y) \qquad (39)$$

with t_n an arbitrary real number and δ the Dirac delta function. The solution for G_{mn} in the far-field is presented in Appendix B. The result is conveniently written in terms of longitudinal (L_{ij}) and transverse (T_{ij}) tensors as

$$4\pi\mu r\, G_{ij} = T_{ij} \exp(-j\omega\, r/c_T) + L_{ij} \exp(-j\omega\, r/c_L) \qquad (40)$$

with c_L and c_T the longitudinal and transverse wave velocities.

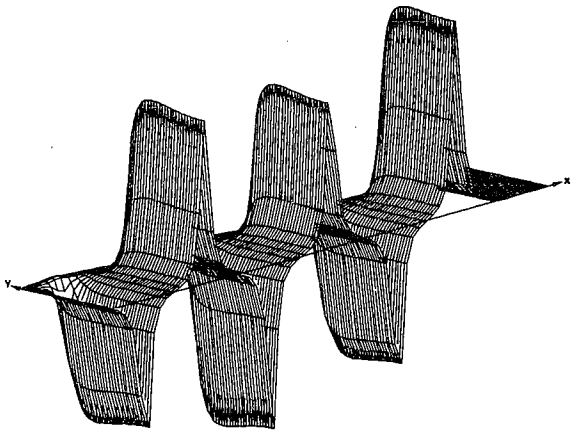

Fig. 12 t_x (x,y) in first quandrant for meander coil EMAT. Transverse (y) scale expanded by a factor of 5.

Define

$$\kappa = c_L/c_T \qquad (41)$$

and use spherical polar coordinates, $z = r\cos\theta$, etc., then, for both $i \neq 3$, and $j \neq 3$,

$$T_{ij} = \delta_{ij} - \hat{r}_i\hat{r}_j \left[4\cos\theta\,(\kappa^{-2} - \sin^2\theta)^{1/2} + 2\sin^2\theta - 1\right]/d_T \quad , \qquad (42)$$

with

$$d_T = (\cos 2\theta)^2 + 4\sin^2\theta\cos\theta\,(\kappa^{-2}-\sin^2\theta)^{1/2} \quad , \qquad (43)$$

and

$$L_{ij} = 2r_i r_j \cos\theta(\kappa^2-\sin^2\theta)^{1/2}/d_L \qquad (44)$$

with

$$d_L = (\kappa^2-2\sin^2\theta)^2 + 4\sin^2\theta\cos\theta\,(\kappa^2-\sin^2\theta)^{1/2} \quad . \qquad (45)$$

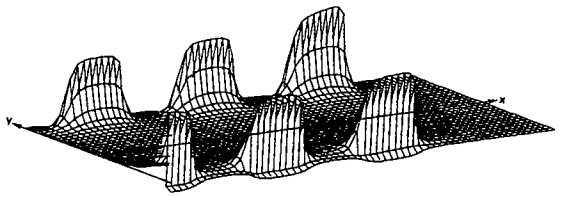

Fig. 13 t_y in right half plane (x20) for meander coil EMAT. Vertical scale as in Fig. 12.

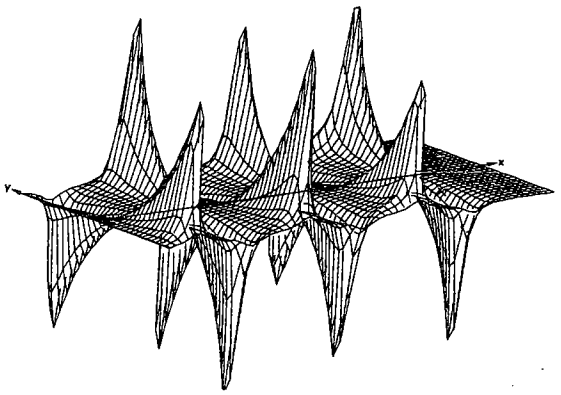

Fig. 14 t_z for meander coil EMAT. All scales as in Fig. 13.

The mixed subscript components (G_{3i}, G_{i3}, $i \neq 3$) are given by

$$T_{i3} = -2\cos^2\theta\, r_i\,(\kappa^{-2}-\sin^2\theta)^{1/2}/d_T \quad , \qquad (46)$$

$$L_{i3} = \cos\theta\, \hat{r}_i\,(\kappa^2-2\sin^2\theta)/d_L \quad , \qquad (47)$$

$$T_{3i} = \cos\theta\, \hat{r}_i\,(2\sin^2\theta - 1)/d_T \quad , \qquad (48)$$

and

$$L_{3i} = 2\cos^2\theta\, \hat{r}_i\,(\kappa^2 - \sin^2\theta)^{1/2}/d_L \quad . \qquad (49)$$

The remaining components of G are obtained from

$$T_{33} = 2\sin^2\theta\cos\theta\,(\kappa^{-2} - \sin^2\theta)^{1/2} \qquad (50)$$

$$L_{33} = \cos^2\theta\ (\kappa^2 - 2\sin^2\theta)/d_L \quad . \tag{51}$$

The square roots arise from the z component of a wave vector and become negative imaginary when their arguments are negative.

It is useful to identify the extent and nature of the polarization of the radiation. SH polarization is defined by a unit vector $\hat{\underset{\sim}{e}}^{(1)}$ perpendicular to both the propagation direction ($\underset{\sim}{r}$, in the far field) and the normal ($\hat{z}$) to the surface. SV polarization is then defined to give a right handed triple by

$$\hat{\underset{\sim}{e}}^{(2)} = \underset{\sim}{r} \times \hat{\underset{\sim}{e}}^{(1)}/r \quad . \tag{52}$$

The displacement of any transverse radiation can then be decomposed into components along these two directions

$$\underset{\sim}{u} = [u^{(1)}\hat{\underset{\sim}{e}}^{(1)} + u^{(2)}\hat{\underset{\sim}{e}}^{(2)}] \exp[j(\omega t - kr)]. \tag{53}$$

In general, $u^{(1)}$ and $u^{(2)}$ will be complex numbers and the polarization will be elliptical. The measurable displacement field will then be given by the real part of $\underset{\sim}{u}$. To describe the properties of the elliptical polarization more conveniently, we define

$$\tau = \omega t - kR \quad , \tag{54}$$

$$\alpha_i = \mathrm{Re}(\hat{\underset{\sim}{e}}^{(i)} \cdot \underset{\sim}{u}\ ) \equiv a_i \cos(\tau + \delta_i) \quad , \tag{55}$$

and

$$\delta = \delta_2 - \delta_1. \tag{56}$$

Here a_i and δ_i can be interpreted as the peak magnitude and phase of the displacements along the SH and axes. α_i is the instantaneous value along the axes. By elimination of τ one then obtains Eq. (12)

$$(\alpha_1/a_1)^2 + (\alpha_2/a_2)^2 - 2\alpha_1\alpha_2/(a_1a_2)\cos\delta = in^2\delta \quad . \tag{57}$$

This quadratic form describes an ellipse, which has the simplified form

$$\sin^2\delta = \lambda_1\beta_1^{\,2} + \lambda_2\beta_2^{\,2} \tag{58}$$

after a rotation of coordinates given by

$$\beta_1 = \alpha_1 \cos\psi + \alpha_2 \sin\psi \tag{59}$$

$$\beta_2 = \alpha_1 \sin\psi + \alpha_2 \cos\psi \tag{60}$$

Here ψ is the angle of the major axis of the elliptical motion, measured with respect to the SH polarization direction $\hat{\underset{\sim}{e}}^{(1)}$, and λ_1 and λ_2 are respectively the semi-major and semi-minor axes of the ellipse. The λ_i are the eigenvalues of the quadratic form and are given by

$$\lambda_i = \frac{1}{2}\left(\frac{1}{a_1^2} + \frac{1}{a_2^2}\right) + (-1)^i\left[\frac{1}{4}\left(\frac{1}{a_1^2} - \frac{1}{a_2^2}\right) \frac{\cos^2\delta}{(a_1a_2)^2}\right]^{1/2} \tag{61}$$

and satisfy

$$0 < \lambda_1 < \lambda_2 \quad . \tag{62}$$

with $\tan\psi = (a_1^{-2} - \lambda_1)\, a_1a_2\sec\delta \quad .$ (63)

β_1 and β_2 are the instantaneous displacements measured along the major and minor axes respectively. Note that $\delta = 0$ implies $\lambda_1 = 0$, and therefore the ellipse equation degenerates to $\beta_2 = 0$, a straight line. Circular polarization results from $\delta = (2n + 1)\pi/2$.

Let us consider the forgoing for the case of radiation from a surface point source oriented in the x direction, $\underset{\sim}{f} = \hat{x}$. The amplitudes $a^{(i)}$ are obtained from $a^{(i)} = \hat{e}_m(i)T_{mi}$, and are given by

$$a^{(1)} = \sin\phi \tag{64}$$

and

$$a^{(2)} = \cos2\Theta\ \cos\theta\ \cos\phi/[\cos^2 2\theta + 4\sin^2\theta\ \cos\theta(\kappa^{-2} - \sin^2\theta)^{1/2}] \quad . \tag{65}$$

For $\theta < \sin^{-1}(\kappa)$ the $a^{(i)}$ are real; the radiation is plane polarized. At $\Theta = \sin^{-1}(\kappa) = \sin^{-1}(1/2)$ = 30° in the example to follow) the amplitude $a^{(2)}$ for SV radiation becomes complex and the radiation becomes, therefore, elliptically polarized. This transition can be appreciated physically by imagining the source to be infinitesimally inside the surface. For $\Theta < \sin^{-1}(\kappa)$ the beam contains SV waves propagating both directly from the source, and reflected from the surface, and to satisfy the boundary conditions on the surface a mode-converted longitudinal wave at $\Theta' = \tan^{-1}[(1 - \kappa^2\sin^2\theta)^{-1/2}]$. At $\Theta = \sin^{-1}(\kappa)$ the mode-converted longitudinal wave becomes evanescent, and the coefficient $u^{(2)}$ concomitantly develops an imaginary part. The phase shift δ is negative; the polarization vector rotates from SH to SV (right-handed). At $\Theta = 45°$ no SV beam can be radiated; the radiation is plane SH. For $\theta > 45°$ a small SV beam reappears with the opposite sign, and thus is left-handed ellipically polarized.

The angle ψ made by the plane of polarization (or of the major axis of the ellipse, depending upon whether $\delta \neq 0$) varies with ϕ as shown in Fig. 15. For small Θ (radiation directed upward) the radiation is plane polarized, varying smoothly

between pure SH at $\phi = 90°$ and pure SV at $\phi = 0$. The discontinuity at $\phi = 0$ occurs because the SH amplitude disappears and reappears reversed symmetrically, as shown.

For θ just below and just below 45° the SV amplitude, because it disappears at 45°, is very small, so, except very close to the forward direction the radiation is nearly pure SH. Since the SV amplitude changes sign at $\theta = 45°$, the angle ψ has a discontinuity of 180° at this point. This discontinuity is essentially one of phase, and obviously does not imply any discontinuity in the amplitudes themselves. The dependence of ψ upon Θ for various planes at fixed ϕ ($x' = x \cos\phi + y \sin\phi$) is shown in Fig. 16.

The power radiated per unit area is most easily obtained from[14]

$$P_n = - v_m \sigma^*_{mn} \quad . \tag{66}$$

and is conveniently separated into SH, SV and L contributions. For the two transverse contributions

$$\underset{\sim}{p}^{(i)} = |a^{(i)}|^2 \mu\omega^2 \underset{\sim}{\hat{r}}/c_T \quad . \tag{67}$$

and for the longitudinal power,

$$\underset{\sim}{p}^{L} = |a^{2}|^2 (\lambda + 2\mu)\omega^2 \underset{\sim}{\hat{r}}/c_L \quad . \tag{68}$$

with

$$\underset{\sim}{a}^{L} = \hat{r}_m u_m \quad . \tag{69}$$

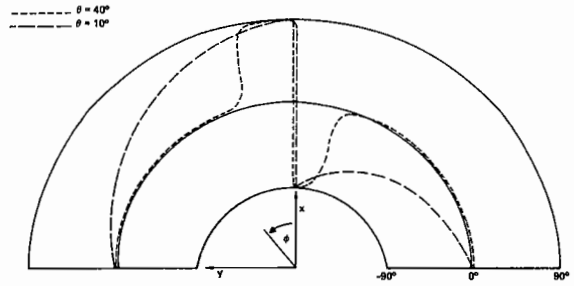

Fig. 15 Polar plot of the angle ψ between q x z [e(SH)] and the plane of the major axis of the possibly degenerate polarization ellipse vs ϕ for various θ.

The SH power radiated into the plane $\Theta = 60°$ by a point force along the x axis is shown in Fig. 17. Obviously, such a force produces no SH radiation in the forward ($\phi = 0$) direction. For fixed ϕ, the radiated SH power is independent of Θ. Figure 18 shows the SV power radiated by the same force into planes at $\phi = 0$, 40°, and 80°. For $\Theta = 90°$ the radiated power is pure SH. The cusp at $\Theta = 30°$ is due to the evanescent mode-converted longitudinal wave described earlier; the null at 45° arises because of reversal in sign of the SV amplitude as is evident from the vectors sketched on Fig. 18. For small Θ(Θ <45°) the x directed force produces a relatively large SV

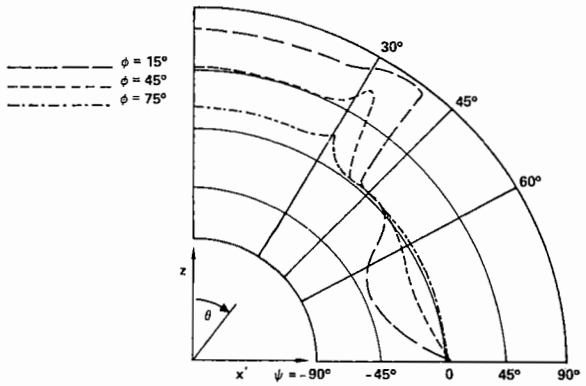

Fig. 16 Polar plot of the angle ψ between q x z [e(SH)] and the plane of the major axis of the polarization ellipse vs θ for various ϕ arising from a point force parallel to x axis.

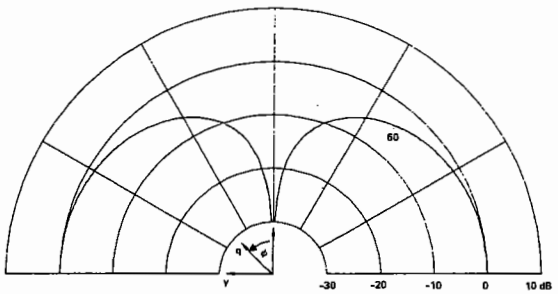

Fig. 17 SH power radiated at $\theta = 60°$ by a point surface force in the x direction.

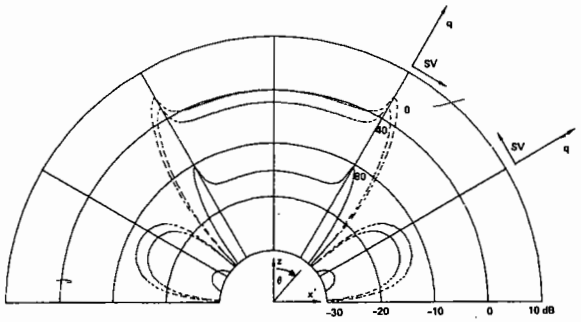

Fig. 18 SV power radiated into the zx' planes by a point force along x axis with $x' = x \cos\phi + y \sin\phi$ for ϕ = 0, 40°, and 80°. Change in sign of the SV amplitude at $\theta = 45°$ is illustrated.

displacement roughly parallel to itself, but for Θ > 45° the SV displacement arises from the x force pushing up the material. This reverses the sign and produces a much lower SV efficiency. This is the origin of the reversal between right elliptically polarized and left elliptically polarized radiation at $\theta = 45°$ The variation of the SV power as a function of ϕ, for $\theta = 30°$ is shown in Fig. 19. The longitudinal power radiated by this x directed point force is shown in Fig. 20 as a function of Θ for various ϕ. It is obvious from symmetry arguments that no longitudinal power will be radiated upward ($\Theta = 0$) by this force, or to

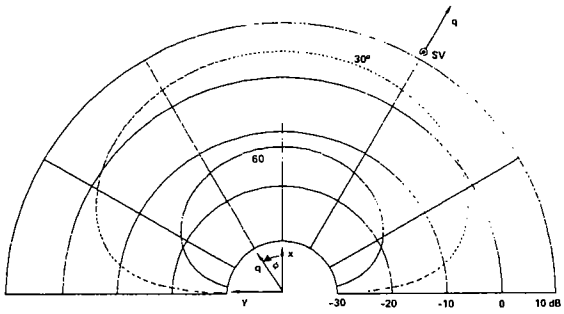

Fig. 19 Cross section of the SV power radiated into planes $\theta = 30°$, $60°$ by a point surface force in x direction.

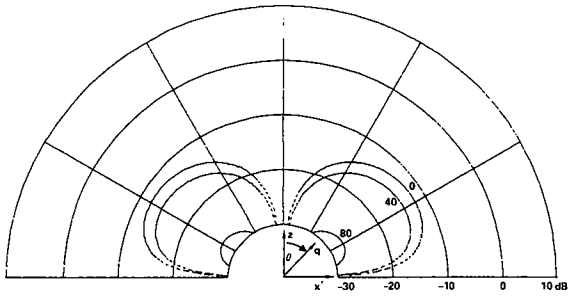

Fig. 20 Longitudinal power radiated into zx' planes ($x' = x\cos\phi + y\sin\phi$) by a point surface force along x axis for $\phi = 0$, $40°$, and $80°$.

the side ($\phi = 90°$). The less obvious fact that the power must vanish for $\theta = 90°$ occurs because such a wave does not satisy the stress free boundary conditions at the half space surface. Figure 21 exhibits the smooth cross section of this longitudinal radiation in the forward direction in the plane $\theta = 60°$.

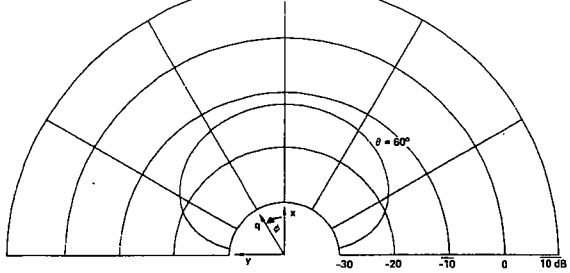

Fig. 21 Cross section in the plane $\theta = 60°$ of the longitudinal power radiated by a point surface force in the x direction.

A point force along the y axis introduces differs from the above only by $\phi \to \phi - 90°$. However, a point force along the z axis is fundamentally different. Note first that such a force produces no SH radiation, and its radiation is independent of ϕ (axially symmetric). The smooth, structureless longitudinal radiation cone is shown in Fig. 22. The SV radiation pattern is more interesting as shown in Fig. 23. Again by symmetry, no SV waves are radiated along the z axis. Furthermore, there is a second null where the direction of the SV radiation vector changes sign at $\theta = \sin^{-1}(\kappa)$. This is again related to

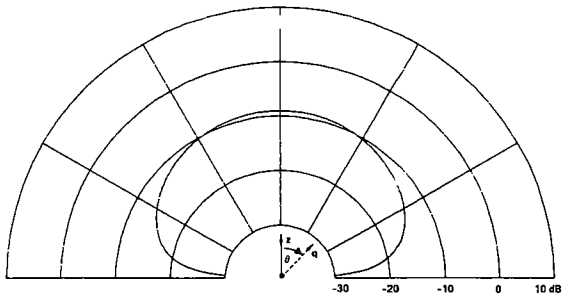

Fig. 22 Longitudinal power radiated by a point surface force along z axis. Pattern is independent of ϕ.

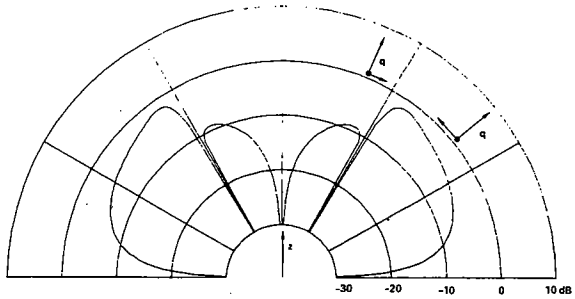

Fig. 23 SV power radiated by a point surface force along z axis. Pattern is axially symmetric.

the previously noted observation that, for a plane SV wave traveling at this angle, the phase matched longitudinal wave is evanescent.

It is interesting to note that numerical comparisons show that the radiation into the planes $\phi = 0$ and $\phi = 90°$ for the force $\underset{\sim}{f} = \hat{\underset{\sim}{x}}$ and into any plane for the force $\underset{\sim}{f} = \hat{\underset{\sim}{z}}$ are equivalent to that for equivalently oriented line forces except for a scaling factor.

EMAT RADIATION PATTERNS

The far field radiation pattern of the EMAT can be obtained from the convolution of the surface tractions t_j with the asymptotic expression G_{ij} for the Green's function,

$$u_i(x,y,z) = \int d^2x' G_{ij}(x - x', y - y', z) t_j(x', y') \quad . \tag{70}$$

This convolution integral can be greatly simplified by working in the far field of the EMAT; i.e., at a distance large compared to the entire EMAT rather than compared to a single EMAT segment. This is only an entirely satisfactory approximation for quite large distances,[14] but a great deal can be learned from it. The effect is to enable us to make replacements

$$|\underset{\sim}{R} - \underset{\sim}{R}'|^{-1}\exp(i\omega|\underset{\sim}{R} - \underset{\sim}{R}'|/c) \simeq r^{-1}\exp(i\omega R/c)$$

$$\exp(-i\underset{\sim}{q}.\underset{\sim}{R}') \quad . \tag{71}$$

This produces the very compact expression

$$4\pi\mu R u_i(\underline{R}) = T_{ij} t_j(\underline{q}_T) \exp(-jq_T R) + L_{ij} t_j(\underline{q}_L) \exp(-jq_L R) \quad (72)$$

where T_{ij} and L_{ij} depend only on θ and ϕ (Eq. 42-51), t_i is the two-dimensional Fourier transform of t_i, $q_T(q_L) = \omega/c_T(c_L)$, and summation on j is implied.

The two-dimensional Fourier transform of t_i needs to be computed only for a rectangular mesh, for which FFT techniques are convenient. The value of t_i is, of course, needed at non-mesh points, but this can be obtained by two-dimensional interpolation without further time consuming integration. An interpolation algorithim was chosen which used a sub-mesh of 16 points (x_n, y_m) surrounding the desired point (x,y) and first fits cubic polynomials to four sets of four points parallel to the x coordinate [$F(x_n, y_1)$, etc.] interpolates in x in each to obtain four new interpolated values $F(x, y_n)$ to which a cubic polynomial interpolation is applied to estimate F(x,y). This was compared to linear (4 mesh points) and quintic (36 mesh points) with excellent results (~0.2% change between cubic and quintic).

We turn to the individual consideration of the three specific transducers. The SH power radiated by the SH EMAT in the xz plane is shown in Fig. 24. At 1.8 mHz this EMAT produces main beams at $\theta = 15°(\phi = 0, 180°)$ and grating lobes at $\theta = 51°(\phi = 0, 180°)$. Note that the beams are very sharp (~3°), and that, without apodization, the side lobes are down the 13 db expected for a linear array of rectangular sources. The cross sections of these beams are shown in Fig. 25. The main beam is very broad (~30°, -3 db), and has two very small side lobes. The grating lobe is 15 db smaller and much narrower (~10°, -3 db). This fact could be used in data analysis to eliminate spurious signals from the grating lobe.

The contamination of the SH beam with SV and longitudinal power is shown quantitatively by the ϕ at which the radiation of that type is largest. The longitudinal power is very small (-28 db) and occurs at a much larger $\theta(\theta = 31°)$, but the SV power occurs at the same angle (with a much different ϕ dependence) and is down only 13 db at peak. Since the generating tractions, t_x and t_z, for the SV radiation are antisymmetric (Table 1) the two lobes of the SV pattern represent amplitudes of opposite sign. It is possible that this antisymmetry could be used in signal processing to reduce the SV contamination further.

Figure 27 illustrates the θ dependence of the SV power radiated by the SV EMAT. The previously noted less-than-optimal aspect ratio of the particular transducer studied here contributes to the large side lobes. A cross section through the main beam at $\theta = 15°$ is shown in Fig. 27.

Figure 29 exhibits the θ dependence of the longitudinal contamination of the predominantly SV

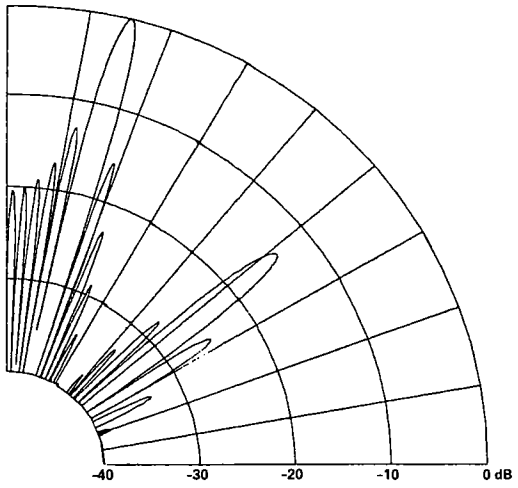

Fig. 24 SH power radiated into the xz plane by the SH EMAT.

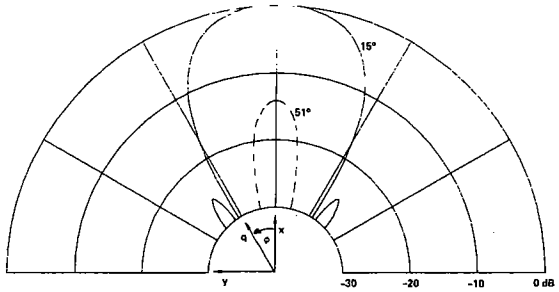

Fig. 25 Cross section of the main beam ($\theta = 15°$) and grating lobe ($\theta = 51°$, dashed curve) of the SH EMAT.

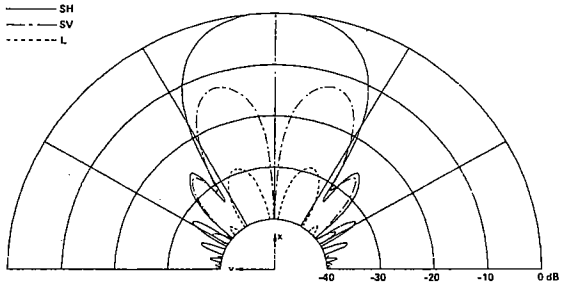

Fig. 26 Dependence upon ϕ of main (SH) and secondary (SV) shear beams at thin maxima ($\theta = 15°$) and of the longitudinal beam at its maximum ($\theta = 31°$) from the SH EMAT.

beam. Cross sections in ϕ of the SH and longitudinal beams from this (SV) transducer are shown in Fig. 30. As with the SV contamination of the beam from the SH transducer, the SH lobes are of opposite sign.

The meander coil (MC) EMAT produces an SV radiation pattern which is narrower in θ, but with very rapid (~3°) variation with θ in the main beam, as shown in Fig. 31.

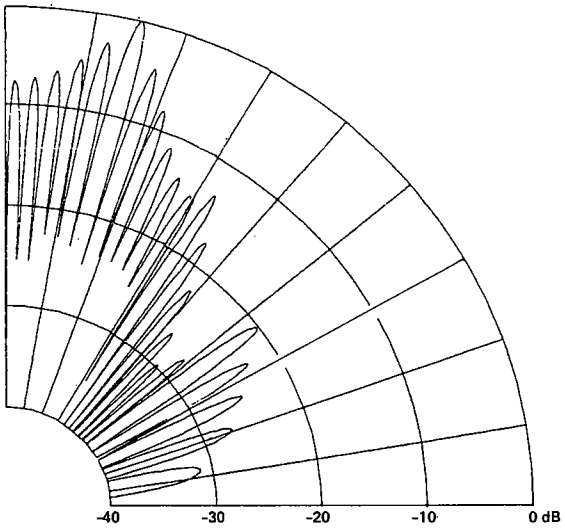

Fig. 27 SV power radiated into the xz plane by the SV EMAT.

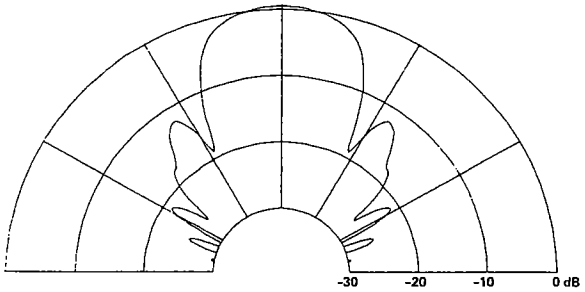

Fig. 28 Cross section of the SV beam radiated at $\theta = 15°$ by the SV EMAT.

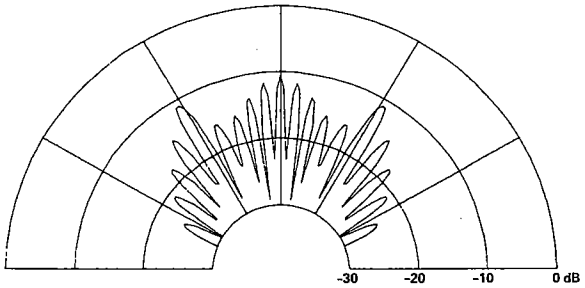

Fig. 29 Theta dependence ($\phi = 0$) of the longitudinal power radiated by the SV transducer into the xz plane.

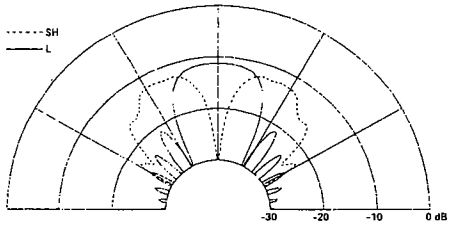

Fig. 30 Cross section (ϕ variation) of SH (dash-dot) and L (solid curve) contamination of beam from SV EMAT.

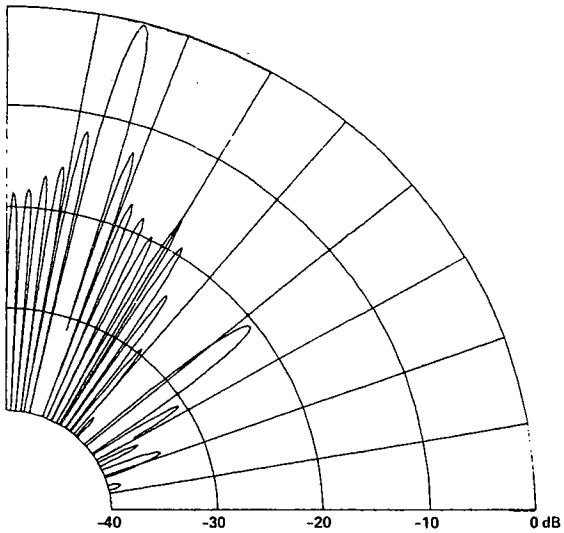

Fig. 31 SV power radiated into the xz plane ($\phi = 0$) by the meander coil EMAT.

The cross-section in ϕ of the main beam is shown in Fig. 32. The irregularities in the radiation pattern shown in Figs. 32, 33, and 34 are apparently due to the loss of numerical accuracy resulting from the coarser mesh required in the absence of symmetry. (Because of mini-computer memory limitations only 2145 elements were stored for each component; for symmetric problems all of these points were in the first quandrant). The (approximate) ϕ dependence of the SH beam from the MC transducer is illustrated in Fig. 33, and that of the longitudinal beam in Fig. 34.

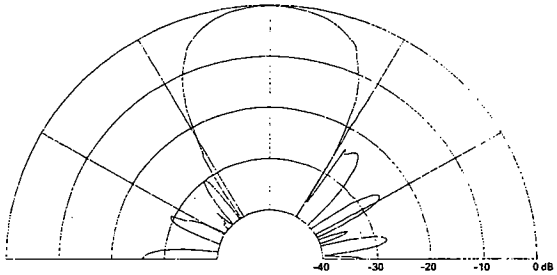

Fig. 32 Cross section of the "main" ($\theta = 15°$) SV beam radiated by the meander coil EMAT.

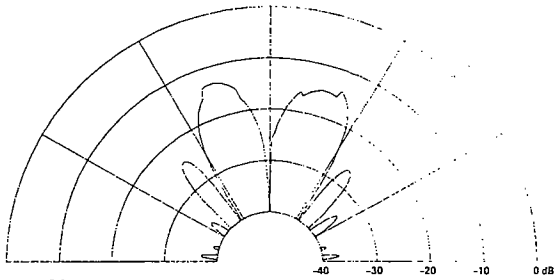

Fig. 33 Cross section of the SH contamination of the beam from the MC EMAT.

CONCLUSIONS

The major results of this paper, in order of decreasing rigor, are the expressions of Section 2 for the eddy currents and magnetic fields produced by various coils and magnets and their concomitant

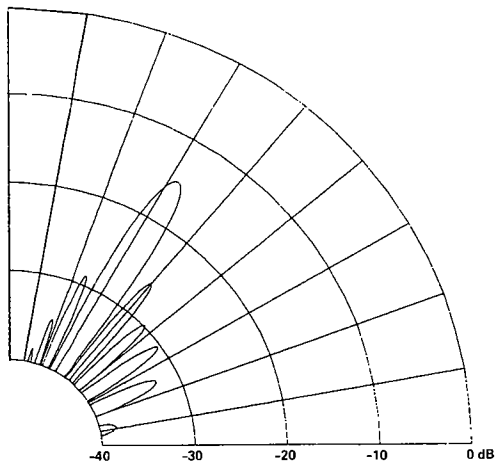

Fig. 34 Longitudinal power radiated into the xz plane by the MC EMAT (ϕ = 0).

surface traction, the three-dimensional far-field half-space response to a point surface force presented in Section 3, and the radiation patterns of the three specific EMAT's in Section 4. The eddy current and magnetic field expressions can be used to generate the surface tractions for a very large set of EMAT's. Those tractions, when combined with suitable other Green's functions can provide, e.g., near or intermediate field radiation, or the radiation pattern in a plate. The simplest improvement would be to eliminate the approximation of Eq. (71), and work in the far field of the point source, which is not nearly as far as the far field for the EMAT. The increase in computational effort is large, however.

The most striking conclusion from the study of the EMAT radiation pattern is the remarkably good behavior of the SH EMAT. The beam is very sharp in θ, very smooth and broad in ϕ, and relatively free from other polarization components. In general, the most useful result of the study is the quantitative information about the lateral (ϕ) variation of the radiation pattern.

APPENDIX

The far field half space surface source Green's Function for the elastic wave equation can be constructed from solutions to the equation

$$[\rho\omega^2 + \mu\nabla^2 + (\lambda + \mu)\,\nabla\nabla]\underset{\sim}{u}^{(r)} = 0 \quad . \qquad (A1)$$

For any real vector $\underset{\sim}{Q}$ with $Q_3 = 0$, there exist three independent solutions $\underset{\sim}{u}^{(r)}$ of the form

$$\underset{\sim}{u}^{(r)} = \hat{\underset{\sim}{e}}^{(r)} \exp\ j(\omega t - \underset{\sim}{Q}\cdot\underset{\sim}{x} - \kappa^{(r)}z] \qquad (A2)$$

where $\kappa^{(r)} = (\omega^2/c^{(r)2} - Q^2)^{1/2}$ with $c^{(1)} = c^{(2)} = c_T$, $c^{(3)} = c_L$. At z = o the surface stresses from an arbitrary linear combination $\underset{\sim}{U}$ of these solutions can be calculated readily. If the combination $\underset{\sim}{U}$ is written

$$\underset{\sim}{U} = j\sum_{r=1}^{3} a^{(r)}\underset{\sim}{u}^{(r)} \qquad (A3)$$

the surface tractions are of the form

$$T_{m3} = j\sum a^{(r)}T_{m3}^{(r)} \quad , \qquad (A4)$$

where $T_{m3}^{(r)}$ are the stresses produced by the solution $u^{(r)}$. For a spatially harmonic applied traction t_m, we require that

$$T_{m3}(x,y,o) = t_m \exp\,[j(\omega t - Q\cdot x)] \quad . \qquad (A5)$$

By integrating the solutions $U(x,y,z;\underset{\sim}{Q})$ over $\underset{\sim}{Q}$ one obtains a solution $\underset{\sim}{W}(x,y,z)$,

$$\underset{\sim}{W} = \int\frac{d^2Q}{(2\pi)^2}\,\underset{\sim}{U}(x,y,z,\underset{\sim}{Q}) \quad , \qquad (A6)$$

which has surface tractions

$$T_{m3}(x,y,o) = \int\frac{d^2Q}{(2\pi)^2}\,T_{m3}(x,y,o) = t_m e^{j\omega t}\delta^{(2)}(\underset{\sim}{x}) \qquad (A7)$$

The $a^{(r)}$ are obtained from combining (A7) with (A4),

$$T_{m3}(x,y,o) = \sum_{r=1}^{3} a^{(r)}(jT_{m3}^{(r)}) \equiv \sum_{r=1}^{3} B_{mr}a^{(r)} \quad . \qquad (A8)$$

The oscillating exponential can be cancelled, and the matrix B in Eq. (A8) inverted to obtain $a^{(r)}$,

$$a^{(r)} = \sum_{m=1}^{3} B^{-1}{}_{rm}t_m \quad . \qquad (A9)$$

This leaves as the displacement field $\underset{\sim}{W}$ whose surface tractions are given by Eq. (A7),

$$W_n = \int\frac{d^2Q}{(2\pi)^2}\sum_{m,r=1}^{3} u_n^{(r)}B^{-1}{}_{rm}t_m \qquad (A10)$$

$$\equiv \sum_{m=1}^{3} G_{nm}(x,y,z)t_m \quad . \qquad (A11)$$

The quality G_{nm} is the displacement field Green's function.

The solutions $\underset{\sim}{u}^{(r)}$ are conveniently chosen with polarization vectors $\hat{\underset{\sim}{e}}^{(r)}$ given by

$$\hat{\underset{\sim}{e}}^{(1)} = (Q_2, -Q_1, 0) \qquad (SH) \qquad (A12)$$

$$\hat{\underset{\sim}{e}}^{(2)} = c_T/(\omega Q)(\kappa_T Q_1, \kappa_T Q_2, -Q^2) \quad (SV) \qquad (A13)$$

and

$$\hat{\underset{\sim}{e}}^{(3)} = (Q_1, Q_2, \kappa_L)c_L/\omega \qquad (L) \qquad (A14)$$

where

$$\kappa_T = (\omega^2/c_T^2 - Q^2)^{1/2} \quad \text{(A15)}$$

and

$$\kappa_L = (\omega^2/c_L^2 - Q^2)^{1/2} \quad \text{(A16)}$$

The surface tractions associated with these modes are given by

$$\underset{\sim}{t}^{(1)} = \chi_m T^{(1)}_{m3} = -\mu j\kappa_T(Q_2, -Q_1, 0)/Q$$

$$\underset{\sim}{t}^{(2)} = -\mu j c_T/(\omega Q)[(\kappa_T^2 - Q^2)Q_1, \quad \text{(16a)}$$

$$(\kappa_T^2 - Q^2)Q_2, -2Q^2\kappa_T) \quad \text{(A17)}$$

and

$$\underset{\sim}{t}^{(3)} = -2\mu j c_L/\omega(\kappa_L Q_L, \kappa_L Q_2, (\tfrac{1}{2}\omega^2/c_T^2 - Q^2)) \quad \text{(A18)}$$

These equations (A16-A18) define the 3 x 3 matrix B_{mr} whose inverse is easily obtained analytically.

No approximations have been made to this point, but now a considerable simplification can be obtained by going to the far field where the integral over $\underset{\sim}{Q}$ can be evaluated approximately by the method of stationary phase. The integral needed is obtained from Eq. A10, A11, and A2,

$$G_{nm}(x,y,z) = j\int \frac{d^2Q}{(2\pi)^2} \sum_{r=1}^{3} \hat{e}^{(r)}_n \exp$$

$$j(\omega t - \underset{\sim}{Q}\cdot\underset{\sim}{x} - \kappa^{(r)}z)\, B^{-1}_{rm} \quad \text{(A19)}$$

We neglect the $\underset{\sim}{Q}$ dependence of $\hat{\underset{\sim}{e}}^{(r)}$ and B^{-1}_{rm} and search for an extremum in the two variables Q_1, Q_2 of the phase ϕ,

$$\phi = \omega t - xQ_1 - yQ_2 - z\,(\omega^2/c^2 - Q_1^2 - Q_2^2)^{1/2} \quad . \quad \text{A20)}$$

The resulting extremum $\underset{\sim}{Q}^o$ is given by

$$Q_1^o = \omega x/(cR) \quad , \quad \text{(A21)}$$

and

$$Q_2^o = \omega y/(cR) \quad . \quad \text{(A22)}$$

The corresponding value of κ, κ^o, satisfies

$$\kappa^o \equiv (\omega^2/c^2 - Q^{o2})^{1/2} = \omega z/(cR) \quad . \quad \text{(A23)}$$

Then the phase ϕ is replaced by ϕ',

$$\phi'(\underset{\sim}{Q}) = \phi(\underset{\sim}{Q}^o) + \tfrac{1}{2}(\underset{\sim}{Q} - \underset{\sim}{Q}^o)_i(\underset{\sim}{Q} - \underset{\sim}{Q}^o)_j \frac{\partial^2\phi}{\partial Q_i \partial Q_j} \quad \text{(A24)}$$

with the second derivatives evaluated at Q^o. The constant phase $\phi(Q^o) = \omega(t - R/c)$ can be removed from the integral. The remaining quadratic exponential cn be integrated as a product of Fresnel integrals after a change of variables to eliminate the cross term, Q_1Q_2. The results have the form

$$\int \frac{d^2Q}{(2\pi)^2} f(\underset{\sim}{Q}) \exp[j\phi(\underset{\sim}{Q})] \sim j\omega \cos\theta \; f(\underset{\sim}{Q}^o)$$

$$\exp[j\omega(t - R/c)]/(4\pi cR) \quad \text{(A25)}$$

Note the integrals in (A19) include both values of $c^{(r)}$, and the integrands must be evaluated at $q^{(r)} = \omega x/c^{(r)}$, where $\underset{\sim}{q} = (Q_1, Q_2, \kappa)$. That is, the approximate Green's function is

$$G_{nm}(x,y,z) = -\frac{\cos\theta\; e^{j\omega t}}{4\pi R} \sum_r q^{(r)} \hat{e}^{(r)}_n$$

$$\exp(-j\omega R/c^{(r)}) B^{-1}_{rm}$$

with $\hat{\underset{\sim}{e}}^{(r)}$ and B^{-1}_{rm} evaluated at $\underset{\sim}{Q} = (\omega/c^{(r)})(x,y,o)/R$ where $R^2 = x^2 + y^2 + z^2$. Straightforward algebra produces the results given in Eq. (42-51).

ACKNOWLEDGEMENT

This research was sponsored in part by the Center for Advanced NDE operated by the Science Center, Rockwell International, for the Advanced Research Projects Agency and the Air Force Materials Laboratory under Contract F33615-74-C-5180.

REFERENCES

1. C.F. Vasile and R.C. Thompson, J. Appl. Phys. 50, 2583 (1979).
2. K. Kawashima, J. Acoust. Soc. Am. 60, 1089 (1976).
3. R.B. Thompson, IEEE Trans. Sonics Ultrasonics SU-20, 340 (1973).
4. T.J. Moran, M.J. Lin, F. Buchholtz, and R.L. Thomas, Rev. Sci. Instrum. 46, 931 (1975).
5. L. Szabo and H.M. Frost, IEEE Trans. Sonics Ultrasonics SU-23, 323 (1976).
6. T.J. Moran and R.M. Panos, J. Appl. Phys. 47, 2225 (1976).
7. W.D. Wallace, Int. J. Nondest. Test 2, 309 (1971).
8. E.R. Dobbs, in Physical Acoustics, edited by W.M. Mason and R.N. Thurston (Academic, N.Y., 1975) X.
9. W. Mohr and P. Holler, IEEE Trans. Sonics Ultrasonics SU-23, 369 (1976).

10. Y.H. Pao and C.C. Mow, Diffraction of Elastic Waves and Dynamic Stress Concentrations (Rand Corp, N.Y., 1973) p. 116 ff.
11. M.R. Gaerttner, W.D. Wallace, and B.W. Maxfield, Phys. Rev. 184, 702 (1969).
12. M. Born and E. Wolf, Principles of Optics, Third edition, 24 (1965) Pergamon Press, N.Y.
13. B.A. Auld, IEEE Transactions on Microwave Theory and Techniques, MTT-17, 800 (1969).
14. A. Erhard, J. Kutzner, H. Wustenberg, "Radiation-Pattern of a Generalized Point-Source Near-To-Far-Field Transition," Proceedings of the International Symposium on New Methods of Non-Destructive Testing of Materials and Their Application, Especially in Nuclear Engineering, Saarbrucken, Germany, Sept. 17-19. (To be published by the Deutsche Gesellschoff fur Zerstoruugsfreie Prufung e.V., Dortmund, W. Germany).